Computational Screening of Transition Metal /p-block Hybrid Electrocatalysts for CO_2 Reduction

Sahithi Ananthaneni*, Rees B Rankin†

September 26, 2019

Abstract

Among all the pollutants in the atmosphere, CO_2 has the highest impact on global warming and with the rising levels of this pollutant, studies on developing various technologies to convert CO_2 into carbon neutral fuels and chemicals have become more valuable. In this work, we present a detailed computational study of electrochemical reduction of CO_2 reduction (CO_2RR) to methane and methanol over different transition metal-p block catalysts using Density Functional Theory calculations. In addition to the catalyst structure, we studied reaction mechanisms using free energy diagrams that explain the product selectivity with respect to the competing hydrogen evolution reaction. Furthermore, we developed scaling relations between all the active C bound intermediate species with ΔG (CO*) and O bound species with ΔG (OH*). The limiting potential lines with ΔG(OH*) as descriptor are much less negative compared to U_L lines with ΔG(CO*) as descriptor indicating that catalyst materials following pathways via OH- bound intermediate species require more negative potentials than CO*HCO* and CO_2 COOH* steps to convert into products. We developed thermodynamic volcano plots with two descriptors; CO* and OH* binding free energies and determined the best catalyst material among the initially investigated catalyst materials expecting this plot will provide guidance to the future work on improving the activity of transition metal-p block catalysts for this important reduction reaction.

Keywords: electrochemical reduction, Density Functional Theory, scaling relations, limiting potential, thermodynamic volcano plots, descriptors ■

*Department of Chemical Engineering, Villanova University

†Department of Chemical Engineering, White Hall, Room 313, Villanova University, 800 E Lancaster Ave, Villanova, PA, USA, Corresponding email: rb.rankin@villanova.edu (Rees B Rankin)

Introduction

Over the past century, carbon dioxide emissions have increased due to over-dependence on fossil fuels as energy sources. It is important to reduce/recycle the amount of CO_2 in the atmosphere to meet the needs of green energy development. Electrochemical reduction of CO_2 (CO_2RR) using heterogeneous catalysts is one of the solutions to convert CO_2 to value-added hydrocarbon fuels such as CH_4, CH_3OH. CO_2RR has become state-of-the-art research because it can produce both low- and high-density compounds which can be used as transportation fuels and commodity chemicals using renewable energy sources as input. However, the reduction of CO_2 is complex as the reaction involves various surface bound reaction intermediates and can form different products for a range of applied potential such as carbon monoxide, formaldehyde, methane, methanol and other C_2+ hydrocarbons. Each reaction follows a reaction pathway involving multi-electron transfer and proceeds through different reaction intermediates. An ideal electrocatalyst must favor desired product formation among different carbon-based products. This desired selectivity when combined by a fact that CO_2 requires more negative potentials to drive the reaction forward due to its high stability under environmental conditions becomes a major challenge. The additional energy supplied for the reaction to move forward, called overpotentials is directly related to the catalyst activity and energy efficiency[1]. The most common type of catalysts explored in studying electroreduction reactions are transition metals and their compounds such as metal complexes as they have vacant orbitals and active d-electrons which energetically help in bonding between intermediate species and surface of the catalyst[2–4].

It is reported from the past theoretical and experimental studies that Cu is the best-known transition metal electrocatalyst to date which can reduce CO_2 to 16 different products[3,5,6]. But this happens at higher overpotentials (~1V) which obstruct this reaction from being an energy efficient process; additionally poor selectivity towards specific desired product(s) formation can necessitate separation of this wide range of products increasing the process inefficiency. Due to these reasons, there has been a shift from pure transition metals to alloys, oxides, and even organic molecules as potential CO_2RR catalysts to overcome the above-mentioned drawbacks[7–9]. Some of these materials are able to produce different products at different applied potentials with higher efficiencies, however the reaction mechanism is still poorly understood/explained. For instance, Cu alloyed with other transition metals show improved activity and reduction of the reaction overpotential compared to pure Cu materials. Cu and compositionally modified Cu materials have intermediate binding strength for CO* species and it is predicted that this could be the reason for the improved catalytic activity for this group of materials[10–14]. Another example is MoS_2, a transition metal /p- block hybrid catalyst which binds CO* weaker than other intermediate species (COOH*, HCO*, COH*) help in further reduction of CO_2 [8,15]. Additional studies on transition metal /p-block materials such as oxides and sulfides have shown improved activity, but we do not have any clear understanding of design rules or reaction mechanisms. The improved activity of this class of materials is also due to the fact that metal/p-block catalysts contain more complex reaction sites around the adsorbate due to the multi-element composition around various high symmetry sites i.e. with both metal site and/or p-block binding site whereas pure transition metals contain adsorption sites associated only with the metal atoms. Motivated by these facts, in this work we study various transition metal/p-block materials such as transition metal oxides (TMO) and sulfides (TMS) as an electrocatalyst candidate(s) for CO_2 reduction to different products at lower potentials without compromising with the performance of the catalyst and selectivity of the products.

Specifically, we study Mo, W, Zn (Zincblende and Wurtzite) oxides and Zn (Zincblende and Wurtzite) sulfides to CO, HCOOH, CH_3OH and CH_4 and highlight two important reactions: CH_4 (methane) and CH_3OH (methanol). We predict product selectivity from free energy diagrams (FEDs) and compute their corresponding reducing potentials and overpotentials for each reaction to proceed forward. This overpotential for each electrochemical reaction is used to determine the catalyst efficiency. The product selectivity is related to the competition between different possible reaction paths, and different reaction pathways show different dependence on intermediate species geometry, binding sites and reducing potentials. We employ scaling relations to unify all intermediate species that bind to the surface via one particular species i.e. the descriptor. Additionally, we use descriptor to pictorially depict and rank the activity of different catalysts in this study by building volcano type activity plots. This volcano plot is very similar to previous studies using CO* and OH* binding free energy as a descriptor and further supports the hypothesis that CO_2 reduction reaction proceeds through COOH* and CO* intermediate species[4]. This analysis allows the reducing potentials of CH_3OH and CH_4 formation on different catalyst materials to be expressed as a function of descriptor binding free energy (CO*). This will further benefit in modifying current catalyst materials or explore new electrocatalysts to identify the ideal catalyst for CO_2RR.

Methods

Theoretical Calculations

We use density functional theory (DFT) to understand reaction thermodynamics occurring on the surface of the catalysts in detail and compare the activity and selectivity of different catalysts materials and their surfaces[16–18]. We perform periodic plane-wave DFT calculations using VASP (Vienna Ab Initio Simulation Package) to calculate all the electronic structure properties such as ground state energies, binding energies[19–24]. We employ Van Der Waals opt-PBE functional to perform these calculations as they do not neglect dispersion forces and are proven to show high accuracy tin determining the adsorption properties of biomolecules, molecular crystals, slab materials and their surfaces[24–27] . All the catalyst surfaces are generated both as two- and four-layer slabs with 12Å of vacuum space in order to minimize the interactions between repeated slabs. Geometries are optimized first on constrained 2-layer slab and the lowest energy adsorption sites for each intermediate species are identified. Energetics calculations are reported for 4-layer thick slabs. Throughout this work, all the electronic structure calculations on each catalyst material and its surface are performed with Fermi smearing of 0.2eV and gamma centered k-point mesh of 2x2x1 with convergence of ground state energies less than 0.05 eV/mole-unit cell w.r.t. k- point sampling[28]. We calculate adsorption properties of each intermediate species on the catalyst materials in two different adsorbate orientations (O closer to the surface, C closer to the surface) on various high-symmetry binding sites such as top, bridge, fcc hollow, hcp hollow sites to find the lowest energy adsorption site. All the binding free energy calculations reported in this manuscript are obtained from the lowest energy conformation of intermediate species identified.

Reaction Network

One of the main challenges in CO_2RR is to convert CO_2 into CH_4 and CH_3OH instead of small molecules like CO. This is because, products like CH_4 require a greater number of proton-electron

transfers (PETs) which result in many energy barriers, largely thermodynamically driven and ultimately land up with lower conversion efficiencies. Furthermore, the electrochemical reduction of CO_2 to these complex molecules comes with high cathode overpotential which again results in low conversion efficiencies. Hence, the overall goal of studying this is to understand and identify how to selectively produce desired product among many of the possible products, while simultaneously doing so at lower overpotentials. In this work, we show CO_2 reduction to four different products: CO, HCOOH, CH_3OH and CH_4. The overall reactions for CO_2 reduction to different products and their equilibrium potentials (Ueq, V vs RHE) are shown in **Table 1** below. In parallel, we also study hydrogen evolution reaction (HER) which could be a possible side reaction during this reduction process as thermodynamically, both HER and CO_2RR occur at an equilibrium potential closer to 0V. This is another challenge in CO_2RR. The following table shows the overall reactions along with their standard reducing potentials and the number of proton-electron pairs (PET) required for the product to be formed.

Reaction	U_{eq} (V vs. RHE)	Number of proton-electrons required
$2(H^+ + e^-) \rightarrow H_2$	0	2
$CO_2 + 2(H^+ + e^-) \rightarrow HCOOH$	-0.02	2
$CO_2 + 2(H^+ + e^-) \rightarrow CO + H_2O$	-0.103	2
$CO_2 + 6(H^+ + e^-) \rightarrow CH_3OH + H_2O$	-0.03	6
$CO_2 + 8(H^+ + e^-) \rightarrow CH_4 + 2H_2O$	0.17	8

Table 1: Overall reactions forCO_2 reduction to different products and their equilibrium potentials (U_{eq}, V vs RHE)

We took advantage of the computational hydrogen electrode (CHE) approach to approximate the reaction free energies of each elementary reaction in the reaction network. This is useful for screening and designing electrocatalysts primarily to understand reaction mechanisms for CO_2RR to CH_4 and CH_3OH. Formation of the above products involve various intermediates with electron transfers in each step. Adsorption energy of each intermediate species relative to the surface of the catalyst determines the preferred pathway. The different reaction networks studied in this work is shown in **Table 2.** Binding energies of the adsorbates are computed using energies of gaseous CO, H_2 and H_2O and DFT energies of each adsorbate on its corresponding catalyst surface given by **Equation 1.**

$$\Delta E_{binding} = E_{DFT} - (E_{surface} + x E_C + y E_H + z E_O) \quad (1)$$

The free energy for each of the reaction in the reaction network is computed using Norskov's standard Computational Hydrogen Electrode (CHE) method[1,29]. We use reverse hydrogen electrode (RHE) as a reference electrode for all the reactions and hence is set to zero. Since it is tedious to computationally calculate the chemical potential of each proton-electron pair, we assume that protons and electrons are in equilibrium with one H_2 molecule at zero potential (U=0), pH=0, T=300K and P (H_2) =1 atm as shown in **Equation 2**.

$$2(H^+ + e^-) \rightarrow H_2 \quad (2)$$

CH_3OH Intermediate product formed after each proton-electron transfer						
path	**First**	**Second**	**Third**	**Fourth**	**Fifth**	**Sixth**
A	COOH*	CO* +H_2O	HCO*	CHOH*	CH_2OH*	CH_3OH
B	COOH*	CO* +H_2O	HCO*	CH_2O*	CH_2OH*	CH_3OH
C	COOH*	CO* +H_2O	HCO*	CH_2O*	CH_3O*	CH_3OH
D	COOH*	CO* +H_2O	COH*	CHOH*	CH_2OH*	CH_3OH

CH_4 Intermediate product formed after each proton-electron transfer								
path	**First**	**Second**	**Third**	**Fourth**	**Fifth**	**Sixth**	**Seventh**	**Eighth**
E	COOH*	CO* +H_2O	HCO*	CHOH*	CH* + H_2O	CH_2*	CH_3*	CH_4
F	COOH*	CO* +H_2O	HCO*	CHOH*	CH_2OH*	CH_2*+ H_2O	CH_3*	CH_4
G	COOH*	CO* +H_2O	HCO*	CH_2O*	CH_2OH*	CH_2*+ H_2O	CH_3*	CH_4
H	COOH*	CO* +H_2O	HCO*	CH_2O*	CH_3O*	CH_4 + O*	OH*	H_2O
I	COOH*	CO* +H_2O	COH*	CHOH*	CH_2OH*	CH_2*+ H_2O	CH_3*	CH_4
J	COOH*	CO* +H_2O	COH*	CHOH*	CH* + H_2O	CH_2*	CH_3*	CH_4
K	COOH*	CO* +H_2O	COH*	C*+ H_2O	CH*	CH_2*	CH_3*	CH_4

Table 2: CO_2 reduction reaction network to CH_3OH and CH_4 formation studied on different catalyst materials in this study.

Binding free energy of each intermediate species on the surface of the catalyst at U=0 corrected by zero-point energies (ZPE) with enthalpy and entropy contributions is calculated using **Equation 3.** The ZPE, enthalpy, and entropy of adsorbed species are obtained from previously determined values as they are assumed to be largely independent of catalyst surface and therefore can be approximated to be the same for all structures for the sake and scope of this work[29,30]. Since an explicit treatment of exact solvent structure is tedious to carry out using DFT methods, we have used the implicit method in VASP with the default dielectric constant of H_2O to calculate solvation energies ($E_{solvation}$). These are generally much less computationally demanding than explicit methods but can reproduce significant results as with explicit methods for O*, OH* bound intermediate species[31,32].

$$\Delta\ (\mathrm{U}=0) = \Delta \mathrm{E}_{rxn} + \Delta \mathrm{ZPE} + \int C_{\mathrm{p}}\, \mathrm{dT} - \mathrm{T}\Delta + E_{solvation} \qquad (3)$$

To calculate free energies at potentials other than 0V, correction factor eU can be applied as shown in **Equation 4** which creates a shift in free energy that contains proton-electron transferred by eU.

$$\Delta\ (\mathrm{U}) = \Delta\ (\mathrm{U}=0) + \mathrm{neU}. \qquad (4)$$

Results

Adsorption energy analysis

Adsorbate interactions described by the term "DFT adsorption energies or binding energies" explain quantitatively how strong or weak the species bind to the surface of the catalyst. This adsorptive property (approximately equivalent to the standard enthalpy of adsorption) allows evaluation of the catalyst activity based on adsorbate geometry, adsorption site symmetry, and adsorption site composition. From the reaction pathway network, we have understood that electronic binding energies of COOH*, CO*, COH*/HCO* are the key reaction intermediate species in determining the product selectivity, reaction pathway and building the free energy profile for each product. Based on the adsorption energies of each of these intermediate species, we have identified few important results. Firstly, when we compare COOH* and OCHO* binding energies, OCHO* is more stable than COOH* by around -0.19 to -1.1 eV on the investigated materials. COOH* binds to the surface via C atom whereas OCHO* binds to the surface via two O atoms. However, the best possible reaction pathway for each product proceeds via COOH* because it minimizes the binding free energy of formation of CO* from third proton-electron transfer. Next while comparing COH* and HCO* binding energies, it is worth noting that HCO* (binds via C and O atoms) stronger than COH*(via C atom) by around -0.3 to -3 eV on the investigated TMOs. This initial analysis does not show any common trend in reaction network whether it follows HCO* or COH* pathway. Third, the adsorption energies of CO* are in the range of -0.38 to -0.95 eV on different materials examined. Tuning the binding energy of the intermediate reactants on the catalyst surface can produce carbon products more efficiently. Following sections will explain the compositional and structural features that can further optimize the desired selectivity to CH_3OH and CH_4.

Methane and Methanol evolution on TMO catalyst materials

We construct free energy diagrams (FEDs) to evaluate the reaction mechanism of CH_3OH and CH_4 from CO_2 on each of the catalyst material, which happens via proton–electron transfer steps. These FEDs provide an overall description of the CO_2RR in terms of thermodynamics. These diagrams determine the lowest reaction pathway, final reaction product and overall reducing potential for each catalyst material. With the electronic binding energies of each intermediate species obtained from finding the lowest energy binding sites, we compute the free energy of formation (ΔG) of each step in the reaction network using the standard computational hydrogen electrode (CHE) approach. We plot FEDs for various reaction networks to find the lowest-energy pathway for each product on each catalyst composition. As we apply more negative voltages, the pathway with the smallest positive rate-limiting step (RLS) will be the first pathway to become exergonic. This pathway will be the best lowest energy reaction pathway for CO_2RR. We have shown the lowest ΔG pathway (FEDs) for each product on different electrocatalysts below. All the free energies of the reactions are calculated relative to CO_2.

MoO_3:

Reaction mechanism (B) is followed on MoO_3 (100) surface for CO_2 reduction to CH_3OH which is shown in **Figure 1** and reaction mechanism (G) is followed for CO_2 reduction to CH_4 as shown in **Figure 2**.The protonation of CO* to the product formation is via oxophilic pathway, i.e., via HCO* species. Calculated onset potential required to reduce CO_2 to methane and methanol are identical on MoO_3 catalyst surface which is -0.66V vs. RHE. The potential determining step for both the products is protonation of CH_2O* to form CH_2OH*. Strong bonding of OH* bound species to surface leads to higher reducing potential requirement for further reduction to CH_3OH and CH_4. At the 6^{th} PET, protonation of CH_2OH* yields CH_3OH as well as CH_2 along the CH_4 pathway with OH* removed as water molecule. Inclusion of solvation energies in electrochemical reduction to CH_3OH and CH_4 modified the reducing potential but not the lowest energy reaction pathway and the rate-limiting step. Addition of solvation energies have minimized the reducing potential from -0.77V to -0.66V vs. RHE. This is because, solvent effect has further stabilized O* and OH* bound intermediates such as HCO*, CH_2O*, CH_2OH* on oxide layers minimizing the overall reducing potential by around 0.1V. Other uphill steps like COOH* reduction to CO*, CH_3OH formation, CH_4 formation which have positive ΔG can progress at lower reducing potentials compared to CH_2OH* reduction. From previous theoretical work, Mo-oxide over-layer have been observed to evolve CH_3OH and CH_4 at -0.86V vs. RHE with OH* to H_2O formation as rate limiting step[33].

WO_3

Reaction mechanism (D) is followed on WO_3 (100) surface for CO_2 reduction to CH_3OH as shown in **Figure 3** and reaction mechanism (J) is followed for CO_2 reduction to CH_4 as shown in **Figure 3.** Protonation of COOH* to CO* is the potential determining step for CH_3OH formation with a reducing potential of -1.54V vs. RHE and protonation of CH_2 to form CH_3 is the rate limiting step for CH_4 formation with a reducing potential of -2.38V vs. RHE. This evidently shows that WO_3 favors CH_3OH over CH_4. The protonation of CO* is via carbophilic pathway, i.e., via COH* species. Interestingly, even with strong O* and OH* adsorption to the oxide surface, protonation of CH_2* is the most uphill step for CH_4 formation. All these binding energy properties are studied with solvation effect in consideration. Inclusion of solvation energies have minimized the reducing potential required for CH_3OH formation by 0.2V by stabilizing CO*, CHOH* and CH_2OH* formation steps and making these steps less uphill. However, presence of solvation effect has increased the reducing potential required for CH_4 formation by ~ 1V. This is because, CH_4 formation follows a pathway via carbon bound species i.e. CH*, CH_2*, CH_3* and presence of solvent didn't show considerable effect on the binding energies of these species. From previous theoretical work, W-oxide over-layer have been observed to evolve CH_3OH at -1.81V vs. RHE with CH_3O* to CH_3OH formation as rate limiting step and CH_4 at -1.7V vs. RHE with OH* to H_2O formation as rate limiting step[33].

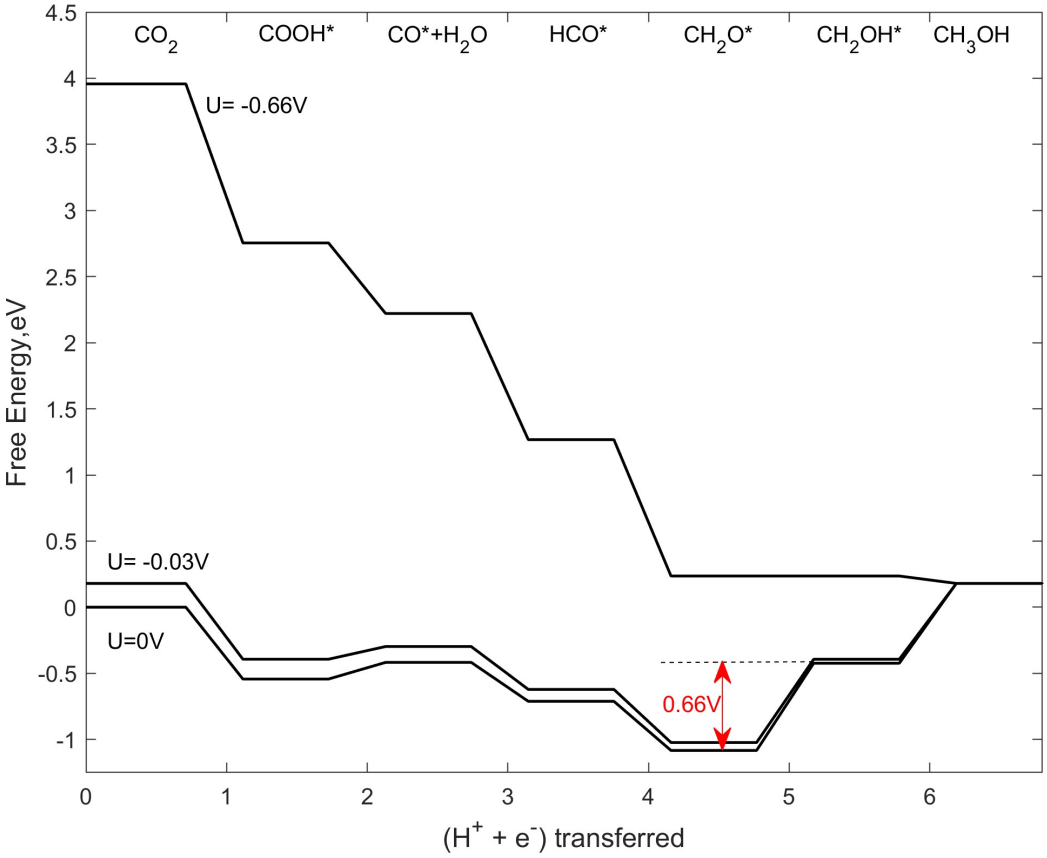

Figure 1: The most favorable pathway for CH_3OH formation at U=0V vs. RHE on MoO_3 catalyst material is shown; The red arrow shows the rate limiting step and the reducing potential required for the reaction to move forward to form CH_3OH. Free energy profiles at limiting potential, U_L vs. RHE where all the steps become exergonic and equilibrium potential U_E vs. RHE are also shown.

ZnO Wurtzite

Reaction mechanism (B) is followed on ZnO-Wurtzite (100) surface for CO_2 reduction to CH_3OH as shown in **Figure 5** and reaction mechanism (G) is followed for CO_2 reduction to CH_4 as shown in **Figure 6**. The protonation of CO* to the product formation is via oxophilic pathway, i.e., via HCO* species. Calculated onset potential required to reduce CO_2 to methane and methanol are identical on this catalyst material which is -0.41V vs. RHE. The potential determining step for both the products is protonation of COOH* to form CO* comparable to the previous theoretical work where CO_2 reduction on ZnO slab with two oxygen vacancies followed a pathway via COOH* to form CO and the energy barrier of this surface reaction was 0.38V and ZnO slab with no oxygen vacancies followed similar pathway with energy barrier of ~1.8V[34]. Similar to the WO_3 catalyst material, inclusion of solvation energies in the electrochemical reduction to CH_3OH and CH_4 has minimized the reducing potential from 0.47V to 0.41V and modified the rate-limiting step from COOH* formation step to CO* formation step but the lowest energy pathway remains unchanged.

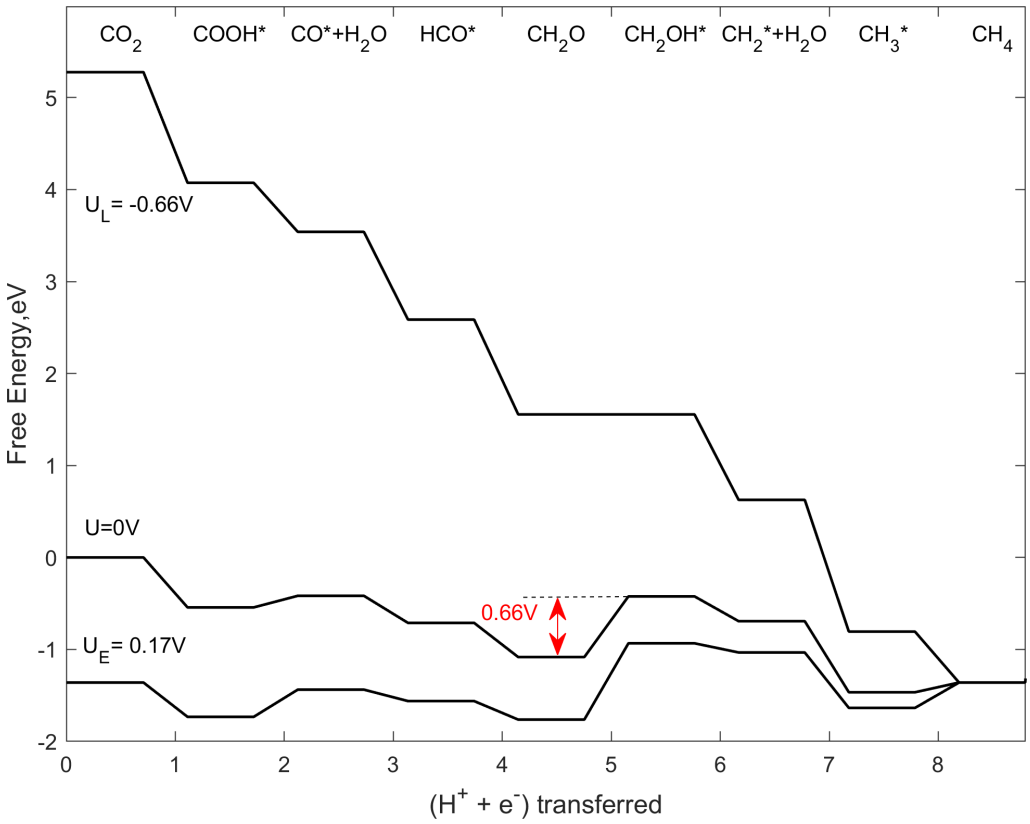

Figure 2: The most favorable pathway for CH_4 formation at U=0V vs. RHE on MoO_3 catalyst material is shown; The red arrow shows the rate limiting step and the reducing potential required for the reaction to move forward to form CH_4. Free energy profiles at limiting potential, U_L vs. RHE where all the steps become exergonic and equilibrium potential U_E vs. RHE are also shown.

ZnO Zincblende:

Reaction mechanism (B) is followed on ZnO-Zincblende (100) surface for CO_2 reduction to CH_3OH as shown in **Figure 7** and reaction mechanism (G) is followed for CO_2 reduction to CH_4 as shown in **Figure 8**. The protonation of CO* in this product formation is via oxophilic pathway, i.e., via HCO* species and this step is the potential determining step for both the products. Calculated limiting potential required to reduce CO_2 to methane and methanol are identical on this catalyst material which is -0.32V vs. RHE. Inclusion of solvation energies in the electrochemical reduction to CH_3OH and CH_4 has minimized the reducing potential from 0.77V to 0.32V by further stabilizing O* and OH* bound species such as HCO*, CH_2O*, CH_2OH* by making them less uphill and also modified the rate limiting step from HCO* protonation step to HCO* formation step. Interestingly, including solvation effect has also modified the lowest energy pathway. At the 4^{th} PET, HCO* protonation favors CH_2O* formation over CHOH* formation and the lowest energy pathway is shifted from (A) to (B) for CH_3OH evolution and (F) to (G) for CH_4evolution.

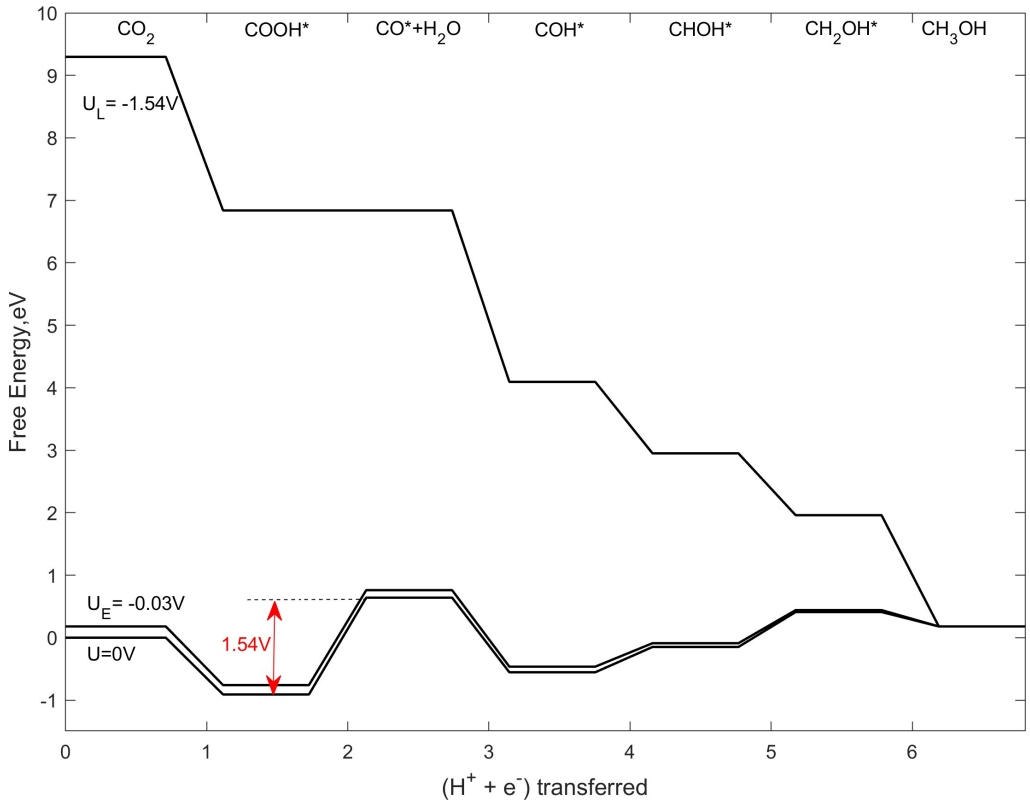

Figure 3: The most favorable pathway for CH_3OH formation at U=0V vs. RHE on WO_3 catalyst material is shown; The red arrow shows the rate limiting step and the reducing potential required for the reaction to move forward to form CH_3OH. Free energy profiles at limiting potential, U_L vs. RHE where all the steps become exergonic and equilibrium potential U_E vs. RHE are also shown.

ZnS Wurtzite:

Reaction mechanism (A) is followed on ZnS-Wurtzite (100) surface for CO_2 reduction to CH_3OH as shown in **Figure 9** and reaction mechanism (F) is followed for CO_2 reduction to CH_4 as shown in **Figure 10**. The protonation of CO* to the product formation is via oxophilic pathway, i.e., via HCO* species. Calculated limiting potential required to reduce CO_2 to methane and methanol are identical on this catalyst material which is -0.57V vs. RHE. Similar to the above binding energy property calculations, inclusion of solvation energies has minimized the limiting potential by ~0.1V for CH_3OH formation by altering the rate limiting step from COOH* protonation step to HCO* protonation step and minimized ~0.05V for CH_4 formation by altering the pathway from to (G) to (F) and rate limiting step from CH_2O* protonation step to HCO* protonation step.

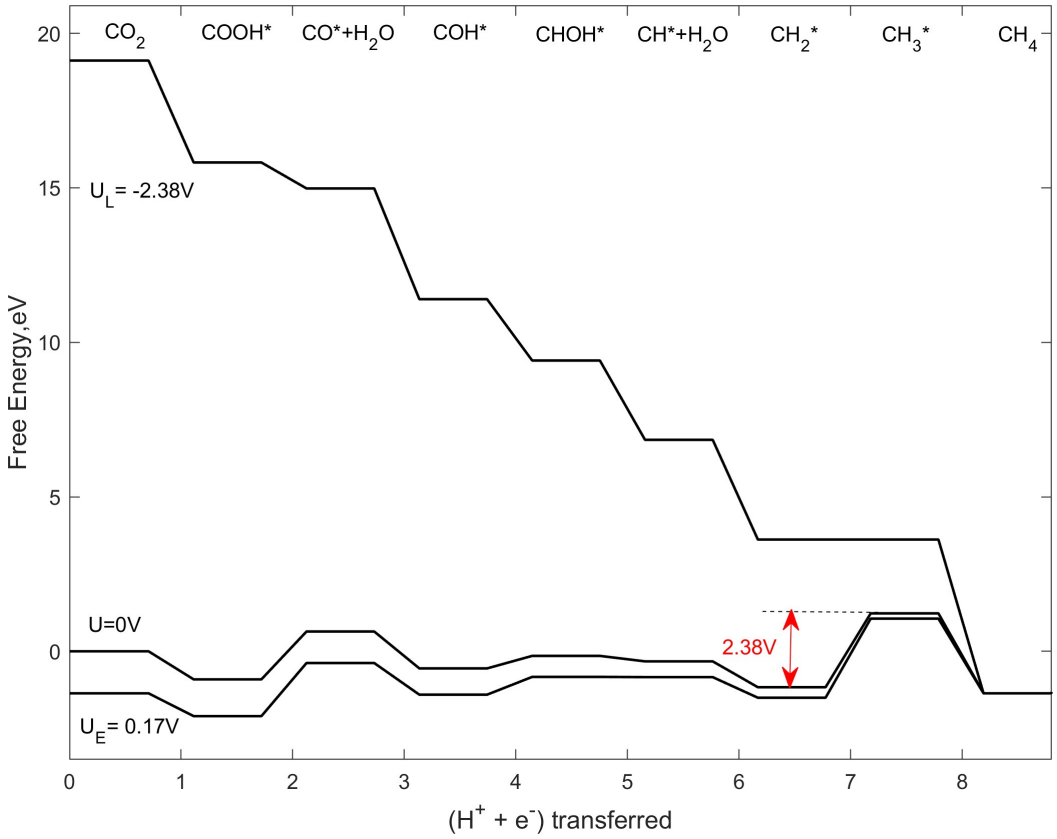

Figure 4: The most favorable pathway for CH_3OH formation at U=0V vs. RHE on WO_3 catalyst material is shown; The red arrow shows the rate limiting step and the reducing potential required for the reaction to move forward to form CH_4. Free energy profiles at limiting potential, U_L vs. RHE where all the steps become exergonic and equilibrium potential UE vs. RHE are also shown.

ZnS Zincblende:

Reaction mechanism (A) is followed on ZnS-Wurtzite (100) surface for CO_2 reduction to CH_3OH as shown in **Figure 11** and reaction mechanism (F) is followed for CO_2 reduction to CH_4 as shown in **Figure 12**. The protonation of CO* to the product formation is via oxophilic pathway, i.e., via HCO* species. Protonation of COOH* to CO* is the potential determining step for CH_4 formation with a reducing potential of -0.66V vs. RHE and protonation of CH_2OH* is the rate limiting step for CH_3OH formation with a reducing potential of -1.26 V vs. RHE. This evidently shows that ZnS Zincblende favors CH_4 over CH_3OH. All these binding energy properties are studied with and without solvation effect in consideration. Interestingly, inclusion of solvation energies have shown an opposite effect by increasing the reducing potential required for CH_3OH formation by 0.6V and CH_4 formation by 0.04V by further stabilizing CO*, HCO*, CH_2OH* formation steps and making these steps more uphill.

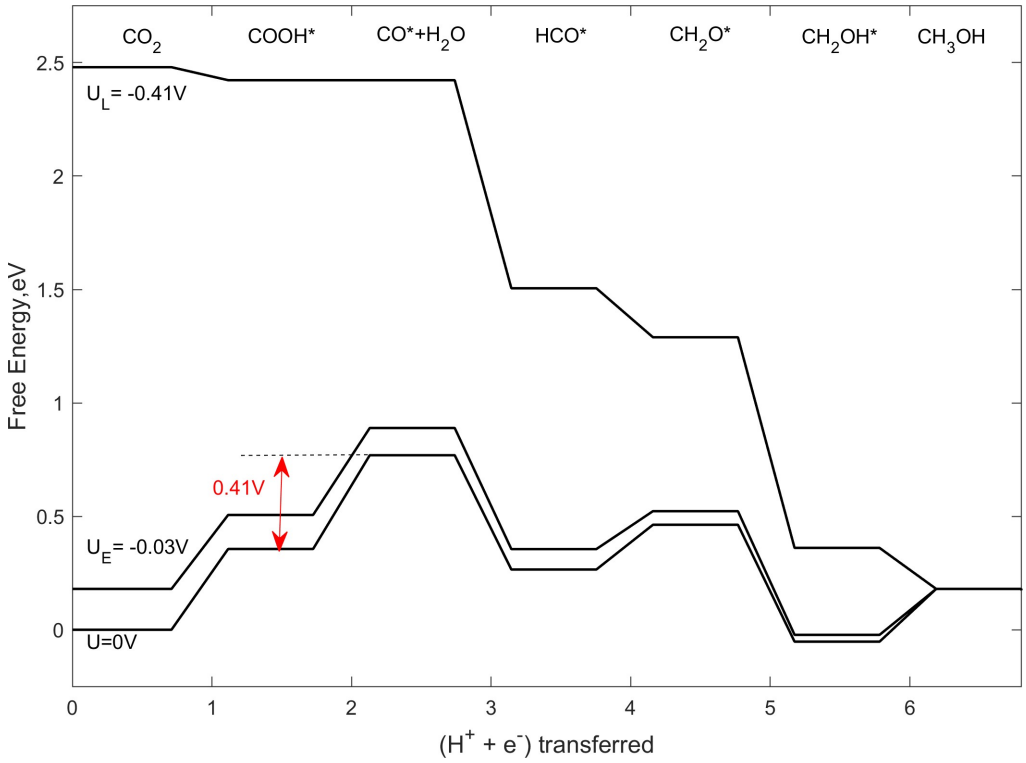

Figure 5: The most favorable pathway for CH_3OH formation at U=0V vs. RHE on ZnO-Wurtzite catalyst material is shown; The red arrow shows the rate limiting step and the reducing potential required for the reaction to move forward to form CH_3OH. Free energy profiles at limiting potential, U_L vs. RHE where all the steps become exergonic and equilibrium potential U_E vs. RHE are also shown.

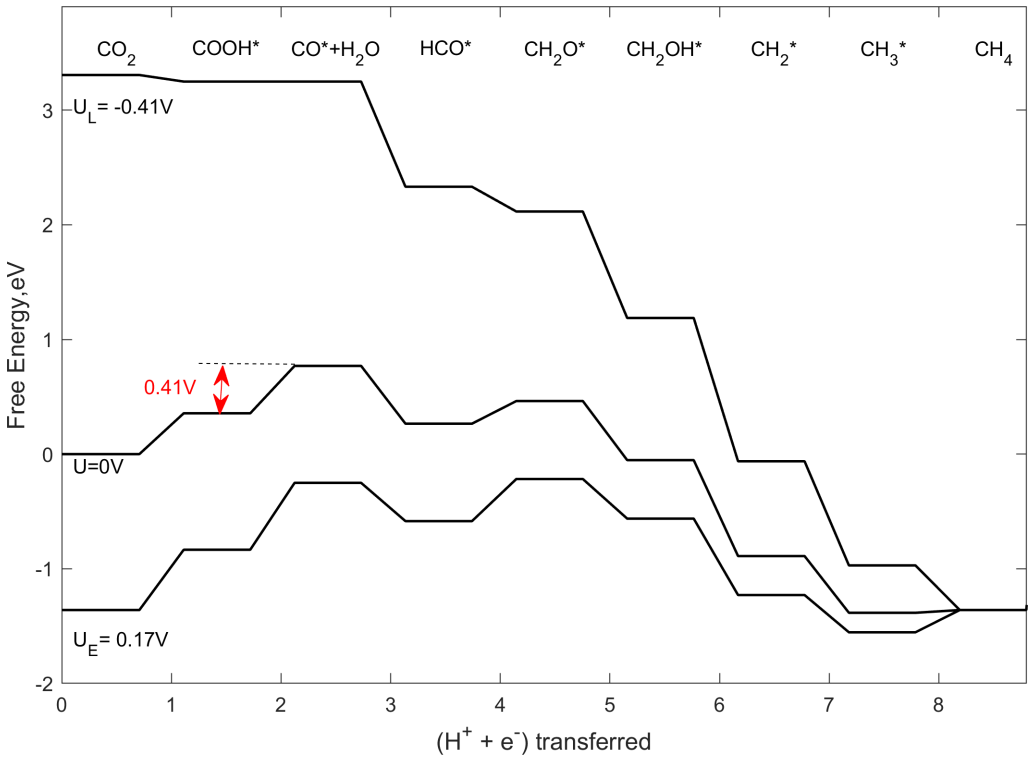

Figure 6: The most favorable pathway for CH_4 formation at U=0V vs. RHE on ZnO-Wurtzite catalyst material is shown; The red arrow shows the rate limiting step and the reducing potential required for the reaction to move forward to form CH_4. Free energy profiles at limiting potential, U_L vs. RHE where all the steps become exergonic and equilibrium potential U_E vs. RHE are also shown.

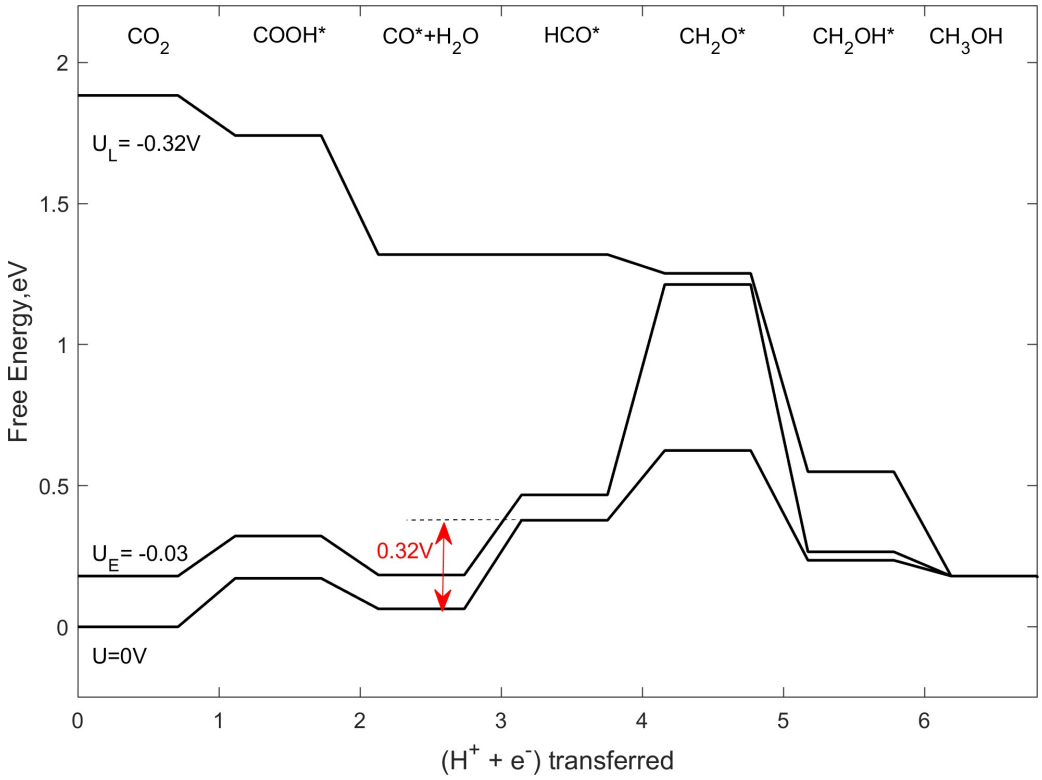

Figure 7: The most favorable pathway for CH_3OH formation at U=0V vs. RHE on ZnO-Zincblende catalyst material is shown; The red arrow shows the rate limiting step and the reducing potential required for the reaction to move forward to form CH_3OH. Free energy profiles at limiting potential, U_L vs. RHE where all the steps become exergonic and equilibrium potential U_E vs. RHE are also shown.

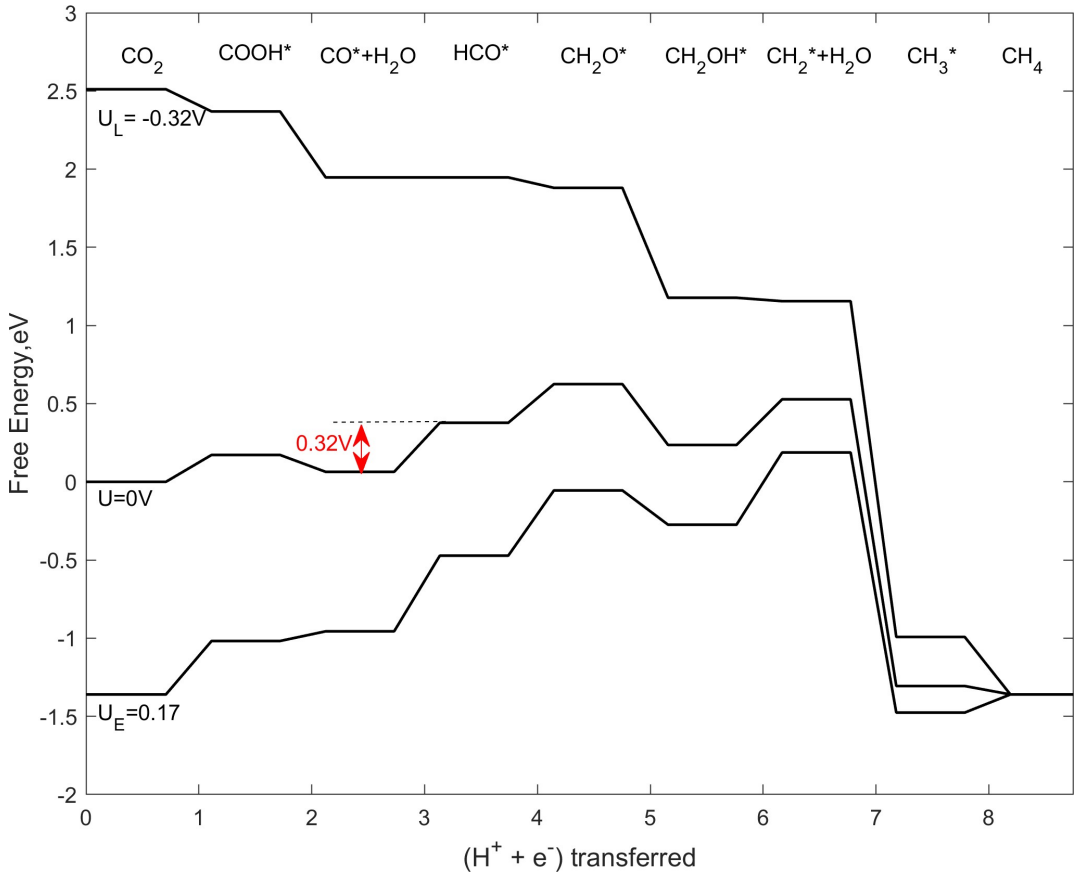

Figure 8: The most favorable pathway for CH_4 formation at U=0V vs. RHE on ZnO- Zincblende catalyst material is shown; The red arrow shows the rate limiting step and the reducing potential required for the reaction to move forward to form CH_4. Free energy profiles at limiting potential, U_L vs. RHE where all the steps become exergonic and equilibrium potential U_E vs. RHE are also shown.

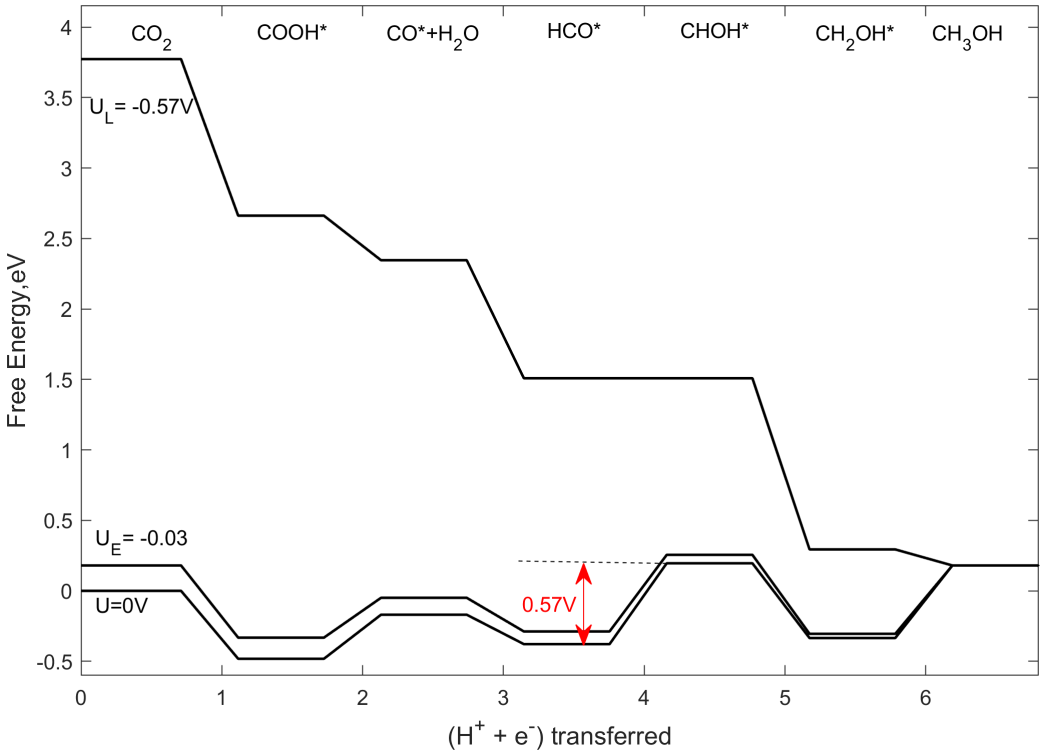

Figure 9: The most favorable pathway for CH_3OH formation at U=0V vs. RHE on ZnS-Wurtzite catalyst material is shown; The red arrow shows the rate limiting step and the reducing potential required for the reaction to move forward to form CH_3OH. Free energy profiles at limiting potential, U_L vs. RHE where all the steps become exergonic and equilibrium potential U_E vs. RHE are also shown.

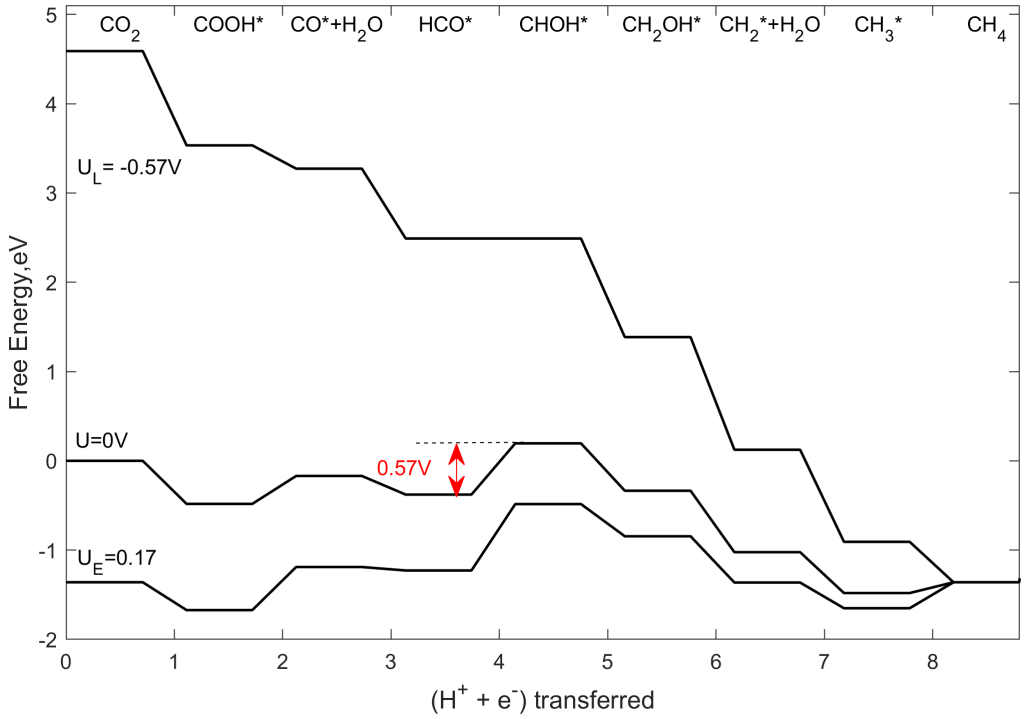

Figure 10: The most favorable pathway for CH_4 formation at U=0V vs. RHE on ZnS- Wurtzite catalyst material is shown; The red arrow shows the rate limiting step and the reducing potential required for the reaction to move forward to form CH_4. Free energy profiles at limiting potential, U_L vs. RHE where all the steps become exergonic and equilibrium potential U_E vs. RHE are also shown.

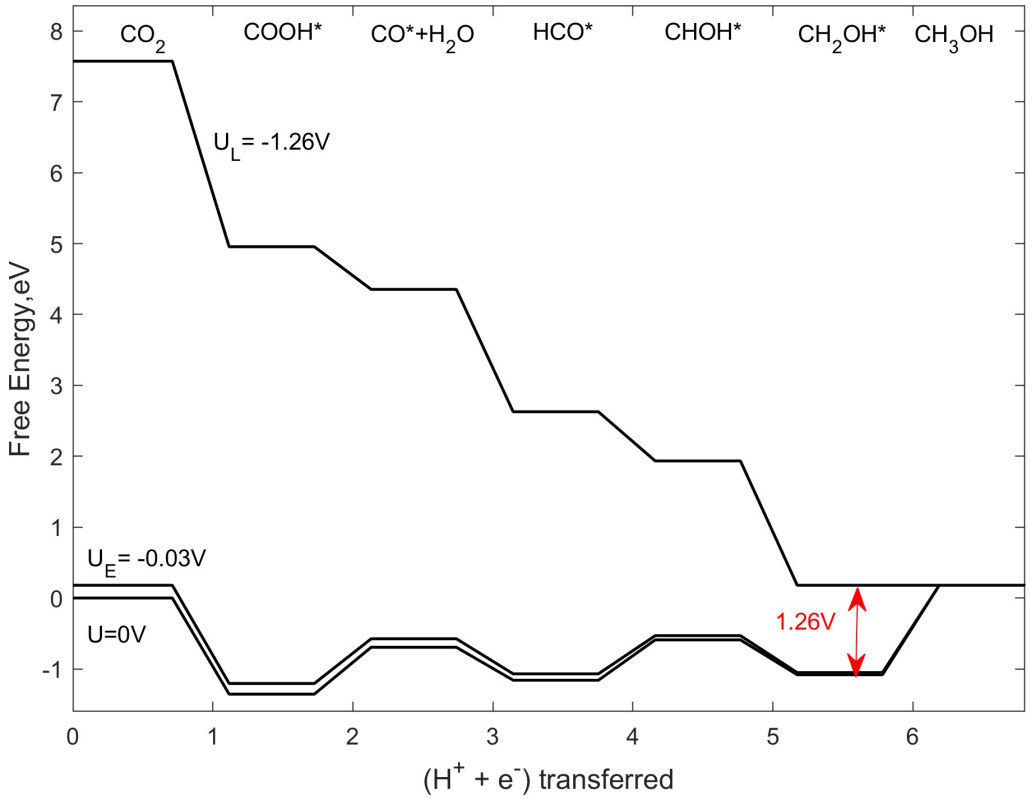

Figure 11: The most favorable pathway for CH_3OH formation at U=0V vs. RHE on ZnS-Zincblende catalyst material is shown; The red arrow shows the rate limiting step and the reducing potential required for the reaction to move forward to form CH_3OH. Free energy profiles at limiting potential, U_L vs. RHE where all the steps become exergonic and equilibrium potential U_E vs. RHE are also shown.

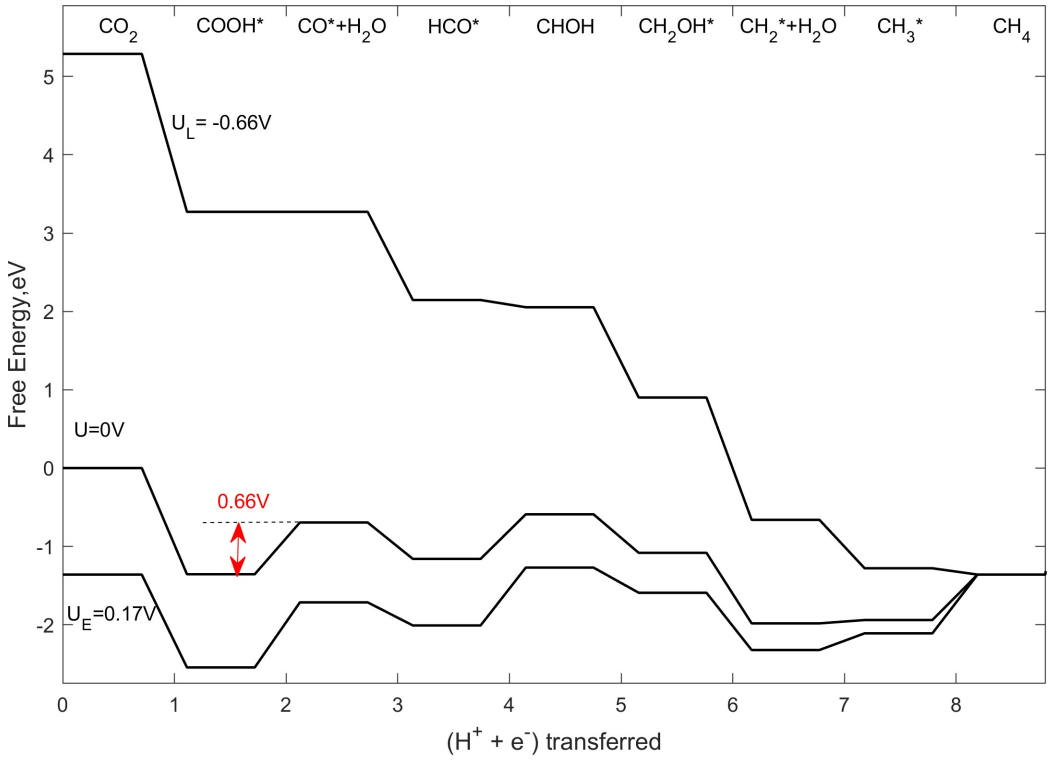

Figure 12: The most favorable pathway for CH_4 formation at U=0V vs. RHE on ZnS- Zincblende catalyst material is shown; The red arrow shows the rate limiting step and the reducing potential required for the reaction to move forward to form CH_4. Free energy profiles at limiting potential, U_L vs. RHE where all the steps become exergonic and equilibrium potential U_E vs. RHE are also shown.

Discussion

Trends in methanol and methane evolution reaction mechanisms on TMOs

The materials considered in this study display a broad range of CO* binding free energies. **Table 3** shows the limiting potential and the rate limiting step for methane and methanol evolution on catalyst materials studied in this work with their corresponding CO* binding free energies which is also called CO* removal potential. Based on ΔG (CO*), we have divided the catalyst materials into three categories. It clearly stands out that, except for WO_3 which follows a different reaction mechanism with very weak CO* binding (>1.0 eV), all other materials have C-O and O-H bound species as rate limiting steps. Surfaces with ΔG (CO*) less than absolute value of 0.5 eV which are MoO_3, ZnO Wurtzite, ZnO Zincblende follow similar type of reaction mechanism for both methane and methanol evolution. However, they have different rate limiting steps as they have different CO* binding strength. And the next group is ZnS materials. Both Wurtzite and Zincblende type of structures have ΔG (CO*) between 0.5eV to 1 eV and follow similar mechanism on both the surfaces for methane and methanol evolution. WO_3 which has weak CO* binding with ΔG (CO*) > 1 eV prefers methanol over methane and ZnS Wurtzite and Zincblende which has ΔG (CO*) between 0.5 eV and 1 eV prefer methane over methanol formation. On the other hand, other catalyst materials which has ΔG (CO*) < 0.5eV in this study prefer both methane and methanol at the same reducing potential.

Catalyst Material	Methanol Limiting potential (V vs. RHE)	RLS	Methane Limiting Potential (V vs. RHE)	RLS	CO* Binding Strength (eV)
MoO_3	-0.66	$CH_2O \rightarrow\rightarrow CH_2OH \rightarrow$	-0.66	$CH_2O \rightarrow\rightarrow CH_2OH \rightarrow$	0.13
WO_3	-1.54	$COOH \rightarrow\rightarrow CO \rightarrow$	-2.38	$CH_2 \rightarrow\rightarrow CH_3 \rightarrow$	1.54
ZnO-Wurtzite	-0.41	$CO \rightarrow\rightarrow HCO \rightarrow$	-0.41	$CO \rightarrow\rightarrow HCO \rightarrow$	0.41
ZnO-Zincblende	-0.32	$CO \rightarrow\rightarrow HCO \rightarrow$	-0.32	$CO \rightarrow\rightarrow HCO \rightarrow$	-0.11
ZnS-Wurtzite	-0.57	$HCO \rightarrow\rightarrow HCOH \rightarrow$	-0.57	$HCO \rightarrow\rightarrow HCOH \rightarrow$	0.53
ZnS-Zincblende	-1.26	$CH_2OH \rightarrow\rightarrow CH_3OH$	-0.66	$COOH \rightarrow\rightarrow CO \rightarrow$	0.66

Table 3: Limiting potential (U_L)and their rate limiting step (RLS) for CH_3OH and CH_4 evolution on catalyst materials studied in this work with their corresponding CO* binding free energies.

Adsorbate scaling relations

On metal catalysts, the binding free energy of CO* and HCO* determine the reducing potential for CO_2 reduction reaction. However, on metal oxide catalysts, other C-O and O-H bound intermediate species such as CO*, HCO*, COOH*, CH_2O*, CH_3O*, CH_2OH* play key role in determining the reducing potential which is also shown in **Table 3** above. We employ linear relationships (scaling relations) between adsorption energies of all intermediate species to unite all the adsorbate species that bind to the surface of the catalyst through particular type of atom(s), descriptor. In this work, a few criteria, such as CO*, OH*, and O* binding free energies, were combined and collectively used to find the activity and selectivity determining descriptor. Our scaling relations has some scatter with r^2 values closer to 1 except for COOH* which has a lower r^2 value. Since we focus more on the importance of trends and qualitative behaviors rather than the exact numeric quantitative accuracy of rate, poor r^2 value of COOH* doesn't change the conclusions reached. Perfect linear scaling relations exist when all the intermediates bind to the sites with same composition like in pure transition metals where the binding sites are associated with only metal atoms, but the effect of composition of binding sites on transition metal-p block materials which are a combination of metal site and p-block atom binding sites results in slight deviation from scaling lines[4,8,15,35–37]. We have divided the 9 key intermediates in our study into two groups. There are 6 key intermediate species (COOH*, CO*, HCO*, COH*, CHOH*, CH_2O*) which interacts with the surface of the catalyst with C atom and 3 key intermediate species (OH*, H_2O, CH_2OH*) which interact with the catalyst surface via O atom. *Using Sabatier's principle, we correlate the limiting potentials required for formation of C bound species as a function of* ΔG *(CO*) and O bound species as a function of* ΔG *(OH*).* All the linear scaling relations calculations for each of these adsorbate species are shown with statistics in the form of linear fit equation in the Section 2 of SI. These relations decrease the dimensionality from nine to two species (CO* and OH*), thereby making the search for trends within transition metal/p-block catalyst materials controllable.

Volcano plots for CH_3OH and CH_4 evolution:

Volcano plots are logical extension of scaling relations which visually represent the relationship between reactivity and activity of various catalysts. The work of Norskov et al. showed that CO* and OH* are the two active descriptors for CO_2RR on transition-metal catalysts[4]. The volcano plots generated with these two species as the descriptors inspired us to divide our active reaction intermediates into two groups as OH bound species and CO bound species. Reactivity, given by the binding free energy of the descriptors CO* and OH*, indicates how strong or weak the catalyst interacts with the intermediate species. Positive values (right leg of the volcano plot) indicate weaker interaction and negative values (left leg) indicate stronger interaction between the reactants and catalyst. In theoretical experiments, activity of a catalyst is typically measured in terms of limiting potential which is the minimum potential required to drive the reaction forward to form desired products. Using Sabatier's principle, an optimal catalyst lies closer to the peak of the volcano and its corresponding value in x-axis is the optimal binding energy of the descriptor (intermediate bond strength) w.r.t. the surface of the catalyst. This gives the maximum reaction rate[38–41]. We build volcano type activity plots using limiting potential required for each elementary reaction step from FED and descriptors (CO* and OH*). With the data analysis we made, volcano plots for each possible product could be prepared i.e. for H_2, HCOOH, CO but for now, our

products of interest are CH_3OH and CH_4. **Figures 13** shows the elementary steps that scale with ΔG (CO*) and **Figure 14 shows** the elementary steps that scale with ΔG (OH*) for CH_3OH and CH_4 evolution. The difference between the equilibrium potential, shown by black solid line in both the figures and the limiting potential of each elementary step is given by theoretical overpotential. In **Figure 13**, at any ΔG (CO*), the most negative limiting potential line which is the bottom-most line determines the theoretical overpotential. The two steps that determine the overpotential of a reaction network via C-O bound species are CO*HCO* and CO_2 COOH* with ZnO- Zincblende material closer to the peak of the volcano. Furthermore, if we look at the CO*HCO* step, the line is nearly horizontal i.e. it is least sensitive to the changes in binding free energy of CO*. This is also because CO* and HCO* scale with a slope 0.87 signifying that the catalyst material which stabilizes the HCO* intermediate also stabilizes CO* intermediate species by almost same amount. This plot is in qualitative agreement with the previous work by of Norskov K. et al. which showed that the materials which expect to follow a reaction network via CO bound species, the binding energies of COOH*, CO*, HCO* dictates the overpotential requirement for the reaction. In the same way, in **Figure 14**, at any ΔG (OH*), the two steps that determine the overpotential of a reaction network via O-H bound species are OH*H_2O and CHOH*CH_2OH with ZnO- Zincblende material closer to the peak of the volcano but still requires a larger overpotential to overcome the rate limiting step. This plot is in qualitative agreement with the previous work of Norskov K. et al. showed that the materials which follow a reaction network via OH bound species and display strong OH binding, OH removal i.e. OH* H_2O dictates the overpotential requirement for the reaction. The limiting potential lines on **Figure 14** are much less negative compared to U_L lines on **Figure 13**. If the materials have high OH affinities, they require higher negative potentials than CO*→HCO* and CO_2→COOH* steps for the OH- bound intermediate species to convert into products. Since CH_3OH and CH_4 share common active intermediates species in their mechanisms, the volcano plots for both the products will be the same except for equilibrium potential (black solid line in **Figure 13** and **Figure 14**) which shifts to 0.03V from 0.17V.

HER:

This unwanted reaction occurs in parallel to CO_2RR. The catalysts for CO_2 electrochemical reduction are also efficient catalysts for HER as thermodynamically both the reactions occur closer to 0V and hence, is a major challenge in the CO_2 electroreduction process. In general, weak H* binding catalysts are more suitable than the strong H* binding catalysts. If the H* binding is too strong to the surface of the catalyst, it can reduce the number of active sites preventing CO_2RR to occur and the only way of removing it under these conditions is to react it off to form H_2. Therefore, an ideal CO_2 reduction catalyst should maintain relatively weak H* binding compared to COOH* as these are the products formed from first PET. In order to understand if CO_2 reduction is preferred over HER on our catalysts materials, we compare binding free energies of COOH* and H*. From **Figure 15**, our work on initially chosen catalyst materials show that COOH* is more stable (more negative ΔG corresponds to stronger binding of the species) when compared to H* providing the opportunity for further reduction to C-H bond formation products even before H* forms H_2. Except for WO_3, which shows relatively large destabilization of H* compared to COOH* which is very stable, it is predicted from FEDs and activity volcano plots that all other catalyst materials have decent selectivity of CH_4 and CH_3OH formation with little hydrogen evolution.

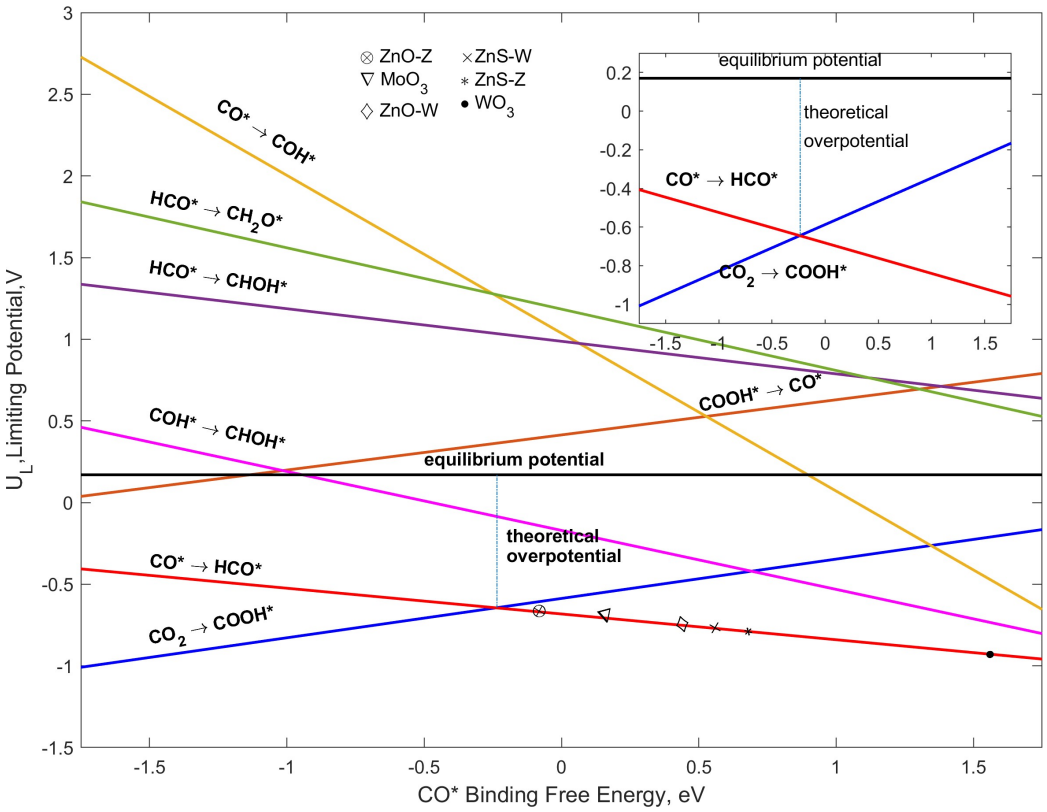

Figure 13: Limiting potentials for the elementary steps in the reaction network vs. ΔG (CO*). Black solid straight line represents the equilibrium potential for CH_4 formation. Vertical blue dotted-line represents the overpotential which is the difference between equilibrium potential and the most negative U_L step. The inset figure shows the two steps CO*HCO*and CO_2 COOH*that generates the peak of the volcano.

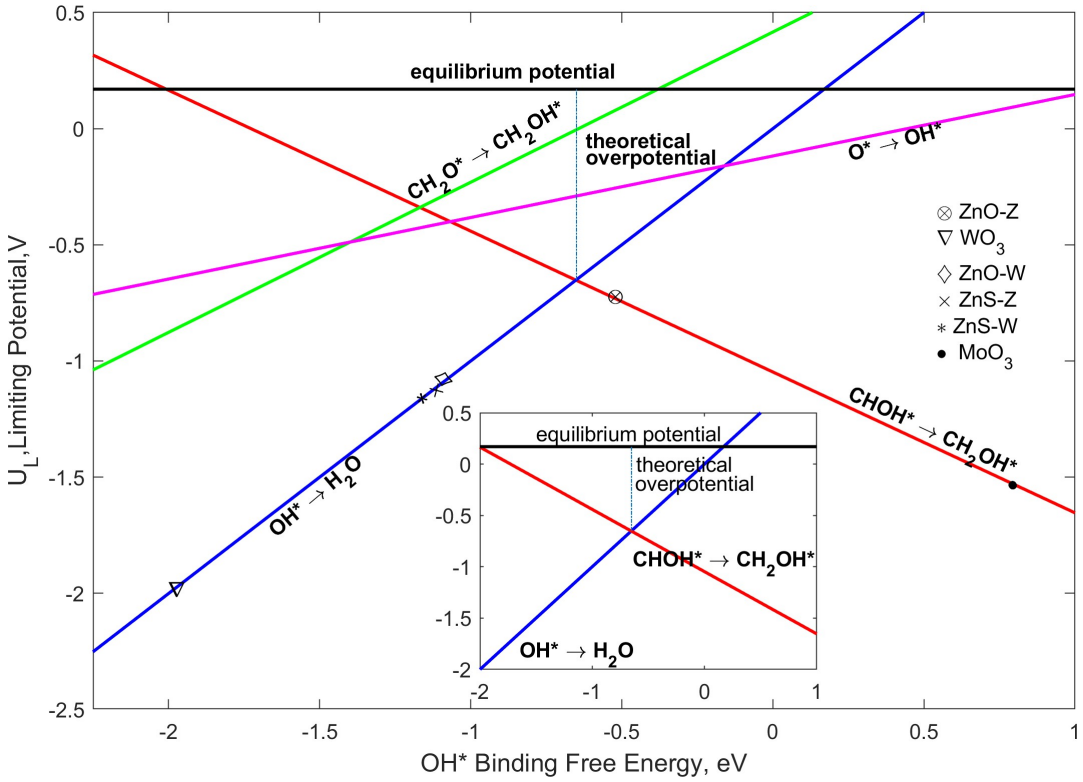

Figure 14: Limiting potentials for the elementary steps in the reaction network vs. ΔG (OH*). Black solid straight line represents the equilibrium potential for CH_4 formation. Vertical blue dotted-line represents the overpotential which is the difference between equilibrium potential and the most negative U_L step. The inset figure shows the two steps OH^*H_2O and $CHOH^*CH_2OH$ that generates the peak of the volcano.

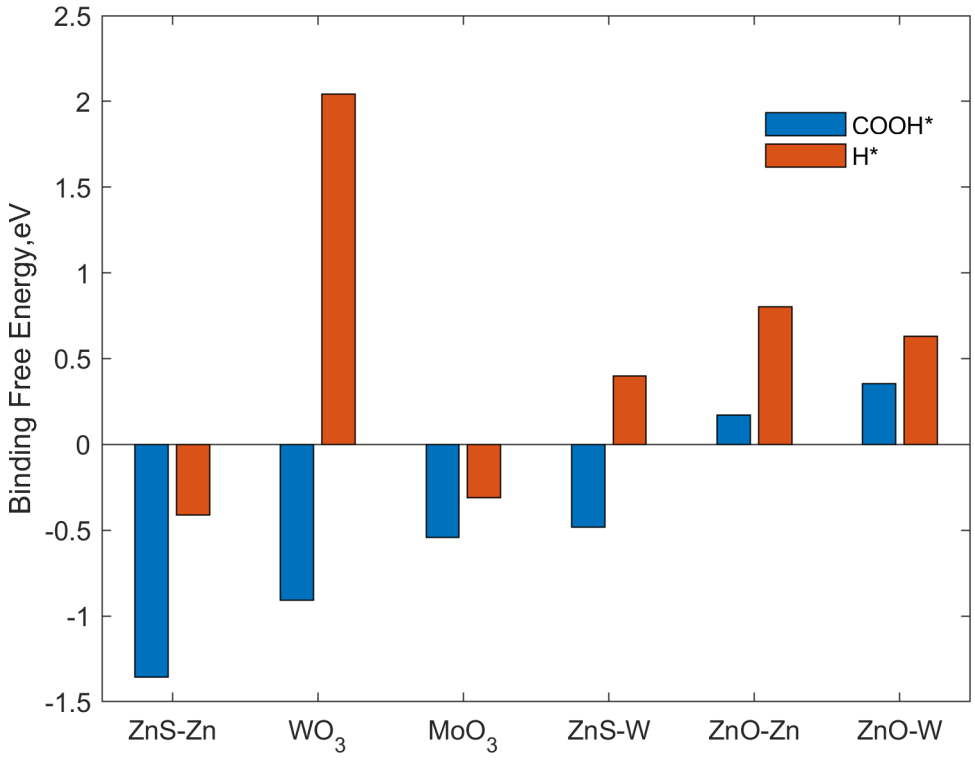

Figure 15: COOH* vs. H* binding free energies on different catalyst materials investigated in this work.

Conclusions

In this report, we investigate the activity and selectivity for the CO_2 reduction reaction (CO_2RR) among six different transition metal-p block catalyst materials: Mo, W, Zn (Zincblende and Wurtzite) oxides and Zn (Zincblende and Wurtzite) sulfides. We predicted the lowest energy pathway for CH_3OH and CH_4 formation from free energy diagrams (FEDs) and computed their corresponding limiting potentials and overpotentials for each reaction to proceed forward. This allowed us to conclude that both methane and methanol share common species in their mechanisms and these species either bind through carbon atom (via CO) or oxygen atom (via OH). We also observed that the solvation effect shouldn't be neglected as this could play an important role in determining the binding energies of species with the surface of the catalyst, in particular for determining the lowest energy pathway followed for CH_3OH and CH_4 evolution. We came to a conclusion that excluding solvation effect especially on oxide surfaces overestimated the binding energies of the key species thereby varying the reducing potential. Therefore, throughout our work, we have taken solvation energies into account to predict the trend in catalyst activity and product selectivity as precisely as possible. We developed scaling relations between all the active C bound intermediate species with ΔG (CO*) and O bound species with ΔG (OH*). The limiting potential lines with ΔG(OH*) as descriptor are much less negative compared to U_L lines with ΔG(CO*) as descriptor indicating that catalyst materials following pathways via OH- bound intermediate species require higher negative potentials than CO*HCO* and CO_2 COOH* steps to convert into products. Additionally, we have also studied HER to identify if CO_2RR is preferred over H_2 formation on initially investigated catalyst materials. It is predicted from FEDs and activity volcano plots, except for WO_3, all other catalyst materials considered in this study have decent selectivity of CH_4 and CH_3OH formation with little hydrogen evolution. To have a deeper understanding of transition-metal /p–block catalysts for CO_2RR, we plan to further extend our work on current catalyst materials by varying com- position, varying surface structure. This will allow us to develop a more comprehensive volcano plot which could further benefit in capturing the trends in CO_2RR using transition metal/p-block catalyst materials.

Acknowledgements

R.B.R. gratefully acknowledges financial and research support from the Department of Chemical Engineering at Villanova University through his startup package fund. S.A. acknowledges financial support from the Department of Chemical Engineering and the College of Engineering at Villanova University as well. Both the authors acknowledge the Center for Nanoscale Materials, an Office of Science user facility, supported by the U.S. Department of Energy, Office of Science, Office of Basic Energy Sciences, under Contract No. DE-AC02-06CH11357 for the use of Carbon cluster to perform calculations requiring high computing power. Both the authors acknowledge assistance from U.N.I.T. team at Villanova University for maintenance of computational resources necessary in this work. Both the authors acknowledge helpful discussions with Tamara Lozano from the Department of Chemical Engineering, Villanova University. R.B.R. and S.A. declare no conflicts ot interest, financial or otherwise.

Supporting Information

A document is available to accompany this manuscript with additional details on results and depictions of surface models.

References

1. Nørskov, J. K., Rossmeisl, J., Logadottir, A., Lindqvist, L., Kitchin, J. R., Bligaard, T., and Jonsson, H., *The Journal of Physical Chemistry B* **2004**, (46), 17 886–17 892.
2. Liu, C., Cundari, T. R., and Wilson, A. K., *The Journal of Physical Chemistry C 2012* (9), 5681–5688.
3. Kuhl, K. P., Cave, E. R., Abram, D. N., and Jaramillo, T. F., *Energy & Environmental Science 2012* (5), 7050–7059.
4. Peterson, A. A. and Nørskov, J. K., *The Journal of Physical Chemistry Letters 2012* (2), 251–258.
5. Yoshio, H., Katsuhei, K., Shin, S., Production, , Co, C. I. E. R. O. C. A. M. E. I. A. H., and Solution, *Chemistry Letters* **1985**, *14* (11), 1695–1698.
6. Liu, X., Xiao, J., Peng, H., Hong, X., Chan, K., and Nørskov, J. K., *Nature communications* **2017**, *8*, 15 438–15 438.
7. Fernández, E. M., Moses, P. G., Toftelund, A., Hansen, H. A., Martínez, J. I., Abild-Pedersen, F., Kleis, J., Hinnemann, B., Rossmeisl, J., and Bligaard, T., *Angewandte Chemie International Edition* **2008**, *47* (25), 4683–4686.
8. Hong, X., Chan, K., Tsai, C., and Nørskov, J. K., *ACS Catalysis* **2016**, *6* (7), 4428–4437.
9. Finn, C., Schnittger, S., Yellowlees, L. J., and Love, J. B., *Chemical Communications* **2012**, *48* (10), 1392–1399.
10. Jia, F., Yu, X., and Zhang, L., *Journal of Power Sources* **2014**, *252*, 85–89.
11. Christophe, J., Doneux, T., and Buess-Herman, C., *Electrocatalysis 2012* (2), 139–146.
12. Rasul, S., Anjum, D. H., Jedidi, A., Minenkov, Y., Cavallo, L., and Takanabe, K., *Angewandte Chemie International Edition* **2015**, *54* (7), 2146–2150.
13. He, J., Johnson, N. J., Huang, A., and Berlinguette, C. P., *ChemSusChem* **2018**, *11* (1), 48–57.
14. Zhao, X., Luo, B., Long, R., Wang, C., and Xiong, Y., *Journal of Materials Chemistry A 2015* (8), 4134–4138.
15. Chan, K., Tsai, C., Hansen, H. A., and Nørskov, J. K., *ChemCatChem* **2014**, *6* (7), 1899–1905.
16. Koch, W. and Holthausen, M. C. **2015**,.
17. Kohn, W., Becke, A. D., and Parr, R. G., *The Journal of Physical Chemistry* **1996**, *100* (31), 12 974–12980.
18. Kohn, W., *Reviews of Modern Physics* **1999**, *71* (5), 1253–1253.
19. Cohen, A. J., Mori-Sánchez, P., and Yang, W., *Science* **2008**, *321* (5890), 792–794.

20. Garrity, K. F., Bennett, J. W., Rabe, K. M., and Vanderbilt, D., *Computational Materials Science* **2014**, *81*, 446–452.

21. Hafner, J. **2007**,.

22. Kresse, G., Furthmüller, J., Software, V., and Vienna, *Phys. Rev. B* **1996**, (11), 169–169.

23. Hafner, J., *Journal of computational chemistry* **2008**, *29* (13), 2044–2078.

24. Piotrowski, M. J., Ungureanu, C. G., Tereshchuk, P., Batista, K. E., Chaves, A. S., Guedes-Sobrinho, D., and Silva, J. L. D., *The Journal of Physical Chemistry C* **2016**, (50), 28 844– 28 856.

25. Gautier, S., Steinmann, S. N., Michel, C., Fleurat-Lessard, P., and Sautet, P., *Physical Chemistry Chemical Physics* **2015**, *17* (43), 28 921–28930.

26. Bucko, T., Hafner, J. R., Lebegue, S., and Angyán, J. G., *The Journal of Physical Chemistry A 2010* (43), 11 814–11824.

27. Klimeš, J. and Michaelides, A., *The Journal of chemical physics 2012* (12), 120 901–120 901.

28. Watson, G., Wells, R. P. K., Willock, D., and Hutchings, G., *Surface science* **2000**, *459* (1-2), 93–103.

29. Peterson, A. A., Abild-Pedersen, F., Studt, F., Rossmeisl, J., and Nørskov, J. K., *Energy & Environmental Science 2010* (9), 1311–1315.

30. Hirunsit, P., *The Journal of Physical Chemistry C* **2013**, (16), 8262–8268.

31. Roux, B. and Simonson, T., *Biophysical chemistry* **1999**, *78* (1-2), 1–20.

32. Cramer, C. J. and Truhlar, D. G., *Chemical Reviews* **1999**, *99* (8), 2161–2200.

33. Tayyebi, E., Hussain, J., Abghoui, Y., and Skúlason, E., *The Journal of Physical Chemistry C* **2018**, (18), 10 078–10 087.

34. Geng, Z., Kong, X., Chen, W., Su, H., Liu, Y., Cai, F., Wang, G., and Zeng, J., *Angewandte Chemie International Edition* **2018**, *57* (21), 6054–6059.

35. Nørskov, J. K., Bligaard, T., Rossmeisl, J., and Christensen, C. H., *Nature chemistry* **2009**, *1* (1), 37–37.

36. Lim, H. K., Shin, H., Goddard, I., Hwang, W. A., Min, Y. J., Kim, B. K., and ., H., *Journal of the American Chemical Society* **2014**, *136* (32), 11 355–11361.

37. Fabbri, E., Habereder, A., Waltar, K., Kötz, R., and Schmidt, T. J., *Catalysis Science & Technology* **2014**, *4* (11), 3800–3821.

38. Nørskov, J. K., Bligaard, T., Logadottir, A., Bahn, S., Hansen, L. B., Bollinger, M., Bengaard, H., Hammer, B., Sljivancanin, Z., and Mavrikakis, M., *Journal of catalysis* **2002**, *209* (2), 275–278.

39. Bligaard, T., Nørskov, J. K., Dahl, S., Matthiesen, J., Christensen, C. H., and Sehested, J., *Journal of catalysis* **2004**, *224* (1), 206–217.

40. Greeley, J. **2016**,.

41. Busch, M., Wodrich, M. D., and Corminboeuf, C., *Chemical science* **2015**, *6* (12), 6754–6761.